Journal of Renewable Materials

Tech Science Press

DOI: 10.32604/jrm.2021.016090

ARTICLE

Constructing Straight Pores and Improving Mechanical Properties of Gangue-Based Porous Ceramics

Hang Xu, Huiling Du*, Le Kang, Qiudi Cheng, Danni Feng and Siyu Xia

School of Materials Science and Engineering, Xi'an University of Science and Technology, Xi'an, 710054, China

*Corresponding Author: Huiling Du. Email: hldu@xust.edu.cn

Received: 05 February 2021 Accepted: 23 March 2021

ABSTRACT

The large-scale accumulation and pollution of solid mining waste is an urgent issue. Coal gangue is a prominent type of solid waste, and shows promise for use in high value-added products due to its content of many important compounds, including SiO_2 and Al_2O_3. This study proposed the preparation of highly porous ceramics from coal gangue, coal slime, and coconut palm fibers. The ceramics were produced at a sintering temperature of 950°C with a fiber content of 6 wt%, which led to the formation of porous ceramics with a porosity of 66.93%, volume density of 1.0329 g/cm^3, compressive strength of 1.1025 MPa, and thermal conductivity is 0.3919 K(W/mk). A finite element model of the porous ceramics was established using the Abaqus module in ANSYS software, where the stress distribution and compressive strength were simulated. Further, the relationship between porosity and compressive strength was analyzed. The thermal properties of the porous ceramics were analyzed using the Fluent module, where the simulated changes in porosity under various sintering temperatures were consistent with the experimental data. The preparation of this highly porous ceramic from solid waste coal gangue shows promise for the minimizing the impact of waste gas and wastewater pollution in the future.

KEYWORDS

Coal gangue; porous ceramics; mechanical properties; thermal properties

1 Introduction

The coal industry has seen rapid development in recent years, which has led to increases in the generation of coal mine solid waste. Coal gangue accounts for the largest proportion of solid waste discharged and stored in coal mines. The accumulative quantity of coal gangue is increasing with increasing coal mining activity [1,2], which has restricted the development of coal chemical enterprises in China. Statistical analysis suggests that coal gangue constitutes 10% to 15% of raw coal production [3], which equates to 368 to 552 million tons generated annually. Further, the total inventory of coal gangue in China is about 4.5 to 5.0 Gt (Giga tons) [4]. The annual utilization rate of coal gangue in China is only ~60% [5]. This mainly involves direct utilization, which does not take advantage of its added value. Accumulated coal gangue occupies a large amount of cultivated land, and can contaminate and pollute soil, groundwater, and rivers with heavy metal ions and potentially toxic substances via the penetration of rainwater [6]. Increased resource utilization of coal gangue relies on the development of high value-added products from this waste stream, which is an important step in current sustainable development strategies.

The main compounds in coal gangue are SiO_2 and Al_2O_3, which are the key substances in the preparation of ceramics, and can replace silicon source and aluminum source. The preparation of porous ceramics from coal gangue is an important route for the development of value-added products. For example, Abdel et al. [7] demonstrated that silicon-rich waste glass, red-clay brick waste, and lead-bearing-sludge can be used to prepare porous materials via foaming to achieve porosities ranging 50% to 89%, where the corresponding bulk densities were 0.73 to 0.27 g/cm^3, thermal conductivities were 0.3 to 0.14 W/mK, and compressive strengths were 3.4 to 14.2 MPa. Han et al. [8] utilized silicon kerf waste and corundum powder to fabricate a silica/mullite porous ceramic via foam-gel casting. The ceramic had a high porosity and low density, where the porosity decreased from 84.1% to 25.45% and the bulk density increased from 0.67 to 1.78 g/cm^3 as the loading increased from 50 to 65 wt%, while the corresponding compressive strength increased from 3.60 to 20.54 MPa and the thermal conductivity increased from 0.204 to 0.892 W/mK. Lü et al. [9] added corn starch to improve the open porosity and pore size of mullite ceramics, where open porosities of 39.67 ± 0.21%, 45.00 ± 0.56%, and 48.12 ± 0.23% were achieved at corn starch contents of 16, 24, and 32 wt%, respectively. However, the mechanical strength degraded from 133.61 ± 6.93 MPa with no corn starch to 66.06 ± 4.79 MPa with 32 wt% corn starch. Liu et al. [10] used $Al(OH)_3$ and coal gangue as primary materials and MoO_3 as an additive to prepare highly porous mullite whisker ceramic microfiltration membranes with a high open porosity of 47.21 ± 0.48%, average pore size of 185.3 nm, and flexural strength of 34 ± 2.5 MPa. However, few studies have investigated the preparation of porous ceramics from coal gangue. Further, the porosity preparation methods that have been previously proposed are too simple, and have mainly been achieved via the addition of a pore-forming agent. The resulting porous ceramics exhibit low porosity, small specific surface area, high density, and weak thermal insulation capability, all of which are not conducive to application in wastewater treatment. The development of porous ceramics with improved porosity and mechanical properties is currently the main challenge in current research.

Mechanical properties play an important role in the overall structure and properties of porous ceramics. The mechanical properties are largely dependent on pore structure and porosity, where an increase in porosity often significantly compromises the mechanical properties. However, the development of porous ceramics with high porosity, low volume density, and good compressive performance is required for waste liquid treatment applications. The regular pore channels in porous ceramics with straight pores allow for orderly arrangement on the ceramic [11], which can effectively improve its compressive performance at a high porosity.

This study used coal gangue and fibers to prepare straight-pore porous ceramics. The related technology and influence of pore pattern and porosity on the mechanical and thermal properties of porous ceramics was investigated. Porous ceramics with different pore patterns and porosities were modelled for mechanical property optimization. Further, the influence of porosity and sintering temperature on the thermal performance of the modelled porous ceramics was investigated.

2 Materials and Methods

2.1 Coal Gangu

Coal gangue (5–6 cm) was crushed (2–3 cm) using a jaw crusher and dried for 12 h at 105°C. The dried gangue was transferred to a planetary ball mill for mechanical grinding, dispersed for 2 h, and sieved to obtain coal gangue powder (<0.1 mm).

2.2 Preparation of Porous Ceramics

Slime (plasticizer) and water (13%–17%) were added to the coal gangue powder in the planetary mill and milled for 2 h at 350 rpm to obtain an even mixture. The mixture was mixed with fibers (2, 4, 6, 8,

and 10 wt%) in a beaker, vacuumed for 30 min, and dried for 4 h at 80°C. Through-holes were prepared via sintering at 900, 950, 1000, 1050, and 1100°C in a high-temperature resistance furnace.

2.3 Characterization

The chemical composition of the coal gangue and coal slime raw materials was determined by the multires-vac28 method in the X-ray fluorescence (XRF; SPECTRO MIDEX, Germany) spectroscopy. The morphology of the materials was characterized using field-emission scanning electron microscopy (FE-SEM; HITACHI S-4800). The phase composition of the porous ceramics sintered at different temperatures was determined using X-ray diffraction (XRD; XRD-6100, Shimazu, Kyoto Co., Ltd., Japan) in a 2θ range of 10° to 80° at a scanning speed of 5 °/min. The thermal properties of the porous ceramics in air were evaluated based on thermogravimetric analysis (TGA) between room temperature and 800°C using a synchronous thermal analyzer (TGA/DSC3+, Mettler Toledo, Shanghai) at a temperature rate of 10 °C/min. The bulk density and porosity of the sintered porous ceramics were measured according to the Archimedes principle. The bending strength was assessed using static and room temperature three-point bending tests at a test span of 20 mm and displacement rate of 0.5 mm using a universal testing machine (REGER, Shenzhen, China). The thermal conductivity of the porous ceramics was tested using a thermal conductivity tester (DRL-III).

2.4 Finite Element Analysis of Porous Ceramics

The mechanical and thermal properties of the porous ceramics were simulated by using the Abaqus and Fluent modules in ANSYS software, respectively. The research object used for modelling was coal gangue porous ceramic with an overall size of 400 μm × 400 μm × 400 μm. The ceramic comprised a variety of pore types, including circular pores (diameter = 40 μm), square pores (40 μm × 40 μm), and strip pores (35 μm × 45 μm). Finite element models of porous ceramics with different types of pores were calculated to analyze the stress characteristics and mechanical properties to determine the most suitable pore type. To simplify the calculations and analysis, it was assumed that (1) the gangue-based porous ceramic included a variety of crystals, which were regarded as a single unit with isotropy, and (2) the elastic modulus of the porous ceramic was 1.39×10^4 N/mm^2 and the Poisson' s ratio was 0.3. (3) Thermal conductivity of coal gangue was 0.68 K(W/mk).

3 Results

3.1 Properties of the Raw Materials

The coal gangue and coal slime were mainly composed of oxygen, silicon, aluminum, iron, calcium, magnesium, potassium, sodium, titanium, vanadium, cobalt, nickel, sulfur, and phosphorus (Tab. 1). The first eight elements accounted for over 98% of the chemical composition of the gangue, where carbon, hydrogen, nitrogen, sulfur, and oxygen typically occurred as organic matter. SiO_2 and Al_2O_3 were the largest components in coal gangue, and served as silicon and aluminum sources for the preparation of porous ceramics.

Table 1: XRF analysis of raw materials

Composition	SiO_2	Al_2O_3	Fe_2O_3	CaO	K_2O	Na_2O	MgO	TiO_2	SO_3	P_2O_5
Coal gangue	52.7	18.1	4.772	1.57	2.51	2.00	1.50	0.748	0.306	0.458
Coal slime	58.29	23.85	4.637	3.62	2.69	1.90	1.51	0.759	0.821	0.369

The XRD pattern of the porous ceramic included peaks at scattering angles of 20.86°, 26.64°, 36.54°, 39.46°, 40.30°, 42.45°, 45.79°, 50.14°, 54.87°, 59.96°, and 68.14°, which were assigned to the (100), (101), (110), (102), (111), (200), (201), (112), (202), (211), (203) crystal planes of quartz (SiO_2, JCPDS Card 46–

1045) (Fig. 1). Further, peaks at 8.74°, 19.76°, and 34.95° corresponded to the (001), (002), and (110) crystal planes of kaolinite ($Al_4[Si_4O_{10}](OH)_8$, JCPDS Card 14–0164), while the peak at 27.88° corresponded to illite $(KH_3O)Al_2Si_3AlO_{10}(OH)_2$, JCPDS Card 02–0056). No peaks attributed to the minor constituents of coal gangue were observed due to their low content [12]. The content of elements melted within the illite decreased at 1000°C, which reduced the intensity of the diffraction peaks, and kaolinite transformation to kaolin initiated at 900°C. Further, the crystal structure of some SiO_2 became amorphous, which reduced the intensity of the corresponding diffraction peaks.

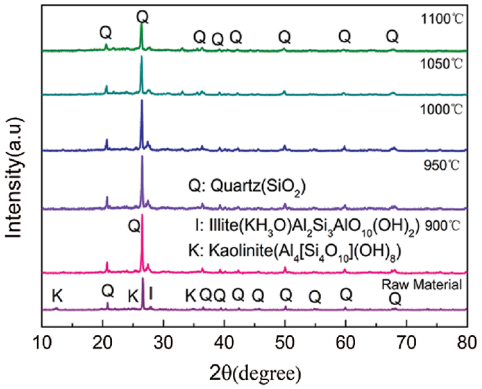

Figure 1: XRD patterns of coal gangue after sintering at various temperatures

The TGA findings provided a better understanding of the combustion characteristics of the raw materials (Fig. 2). The first stage of mass loss of the coal gangue occurred between 350 and 600°C, which was mainly attributed to depolymerization and decomposition of the organic matter and macromolecular material to form gas and tar. The decomposition of mineral matter and further liberation of condensed/polymerized water from the Si–OH and Al–OH groups also occurred in this temperature range [13]. The second stage of mass loss occurred between 600 and 800°C due to the combustion of unburnt carbon in coal gangue and decomposition of carbonate species [14]. The thermal decomposition of natural fibers occurs in three steps. The first step involves dehydration at 105°C due to the evaporation of free water and crystal water in the fiber. The second step between 150 and 300°C is the slow and endothermic weakening of the bonds between the fiber components, as well as gas dispersion due to the degradation of hemicellulose and cellulose. The third step occurs as the temperature exceeds 300°C, where the TGA curve drops significantly. This is most likely associated with cellulose and lignin degradation, where complete decomposition occurs by a maximum temperature of 430°C [15,16].

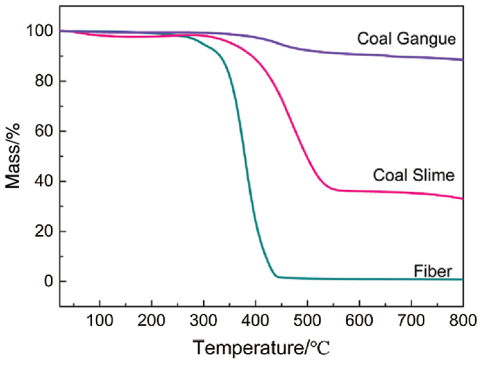

Figure 2: TG curves of the various raw materials

3.2 Microstructure of the Porous Ceramic

The fiber surface was smooth, continuous, and homogenous (Fig. 3a), where these features were clearly observed at low and high magnification. The sintered ceramic exhibited pores formed due to fiber combustion at 950°C, which were straight, regular, and cylindrical (Fig. 3b). The particles on the outer surface of the pores melted, and the liquid glass phase adhered to the surface around the pore. This wetting of the surface particles promoted the contact reaction, thereby compacting the surface [17]. Simultaneously, the conversion of kaolin to metakaolin at 950°C increased the SiO_2 content, which led to strong inter-particle bonding. The adjacent particles were pulled closer together, thereby facilitating partial densification of the porous ceramic via viscous flow [18,19]. The fiber was elongated and had low surface energy, which led to a higher viscosity. This hindered atom diffusion and mass transfer during sintering, resulting in less volume shrinkage and larger porosity [20]. Cross-sectional observation of the porous ceramic revealed that the inner surface was relatively rough (Fig. 3c) with a large number of small pores (Fig. 3d). This may be attributed to the elimination of volatile substances from the fibers during thermal degradation, which resulted in the formation of porous arrays on the fiber walls and further impregnation of the internal channel surfaces. The three-dimensional network of micropores formed on the surface of the channels highlighted the possible multiscale morphology of the fiber [21]. The roughness of the inner surface of the pores was caused by grain growth of the ceramic during sintering, as sintering led to decreased lattice deformation of various materials, uneven grain growth, structural anisotropy, and random orientations within the structure [22]. A rough surface was formed on the inner surface of the pores, which improved the water absorption performance of the ceramic [23].

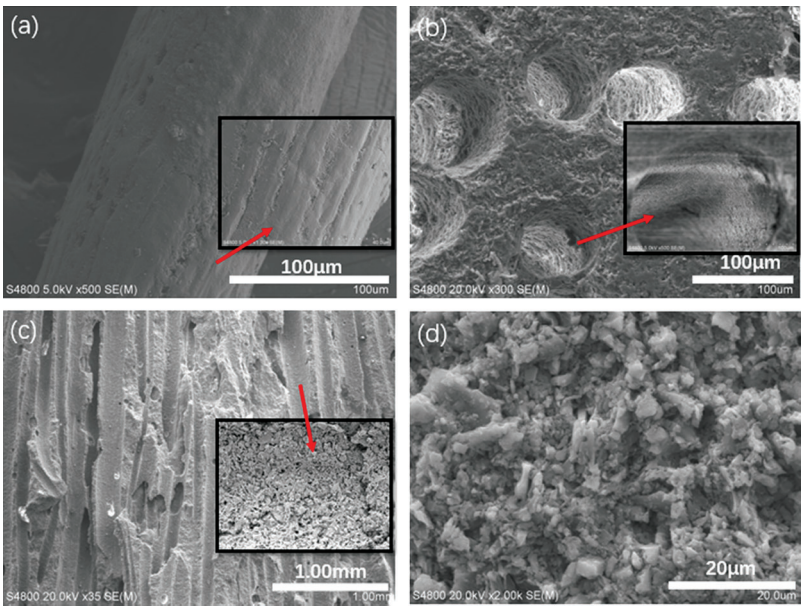

Figure 3: Surface morphology of the fibers and porous ceramics. (a) fiber, (b) pores, (c) cross section, (d) inner surface

3.3 Compressive Properties of the Porous Ceramic

3.3.1 Failure Criteria

The second strength theory assumes that the maximum elongation linear strain is the main factor causing fracture. Regardless of the stress state, brittle fracture will occur when the maximum elongation linear strain (ε_1) reaches the limit value under the unidirectional stress state (ε_u). This is described by Hooke's law:

$$\varepsilon_u = \frac{\sigma_b}{E} \tag{1}$$

where ε_u is the ultimate tensile strain under unidirectional stress, σ_b is the normal stress strength of the cross-section at uniaxial tension breakage, and E is the elastic modulus. Therefore, the brittle failure condition of the material can be expressed as:

$$\varepsilon_1 = \varepsilon_u = \frac{\sigma_b}{E} \tag{2}$$

where ε_1 is the maximum tensile strain.

The test results were in good agreement with the maximum tensile strain theory of brittle materials when the compressive stress exceeded the tensile stress under biaxial tensile stress. Thus, this theory is applicable to the brittle porous ceramic produced from coal gangue when evaluated along its longitudinal section.

3.3.2 Finite Element Analysis of Mechanical Properties of Porous Ceramics

Fig. 4 shows porous ceramic models with three different pore types, and the stress analysis is conducted. The *z*-direction force diagrams for the three different pore types are given in Fig. 5. Stress was transferred from top to bottom, and the amount of deformation decreased step by step from top to bottom. The strip pores had the greatest stress value, while that of the circular pores was much smaller than the others (Tab. 2). These findings demonstrated that pore type is an important factor regarding the stress of porous ceramics, where circular pores allow for superior mechanical properties compared to square and strip types.

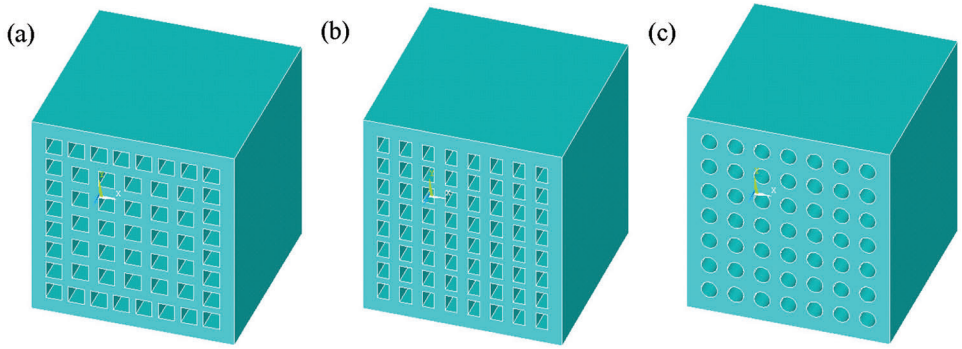

Figure 4: Finite element models of square (a), strip (b), circular (c) pores

3.3.3 Effect of Porosity on Compressive Properties

The porosity gradually increased with increasing fiber content until 6 wt% at 950°C, where minimum and maximum porosities of 55.74% and 66.93% were achieved at 2 and 6 wt% (Fig. 6a). At fiber contents above 6 wt%, the porosity began to decrease due to the excessive fiber content, which caused thinning of the pore walls and partial collapse of the pore structure after sintering. The bulk density of a porous ceramic is closely related to its porosity, where a higher porosity typically corresponds to a lower bulk density [8]. A minimum volume density of 1.0329 g/cm^3 was achieved at 6 wt% fiber, which was consistent with the observed microstructure and pore properties. Burn-out of organic additives and moisture loss were the main causes of linear shrinkage [24]. Thus, linear shrinkage was influenced by the added natural fibers. Porosity increased with increasing fiber content, and the linear shrinkage gradually increased accordingly from 3.49% to 4.05%. Specifically, the linear relationship between linear shrinkage (y) and fiber content (x) was approximated as $y = 0.0695x + 3.367$ with a linear correlation coefficient (R^2) of 0.9862. Thus, the densification phenomenon was governed by the natural fiber content.

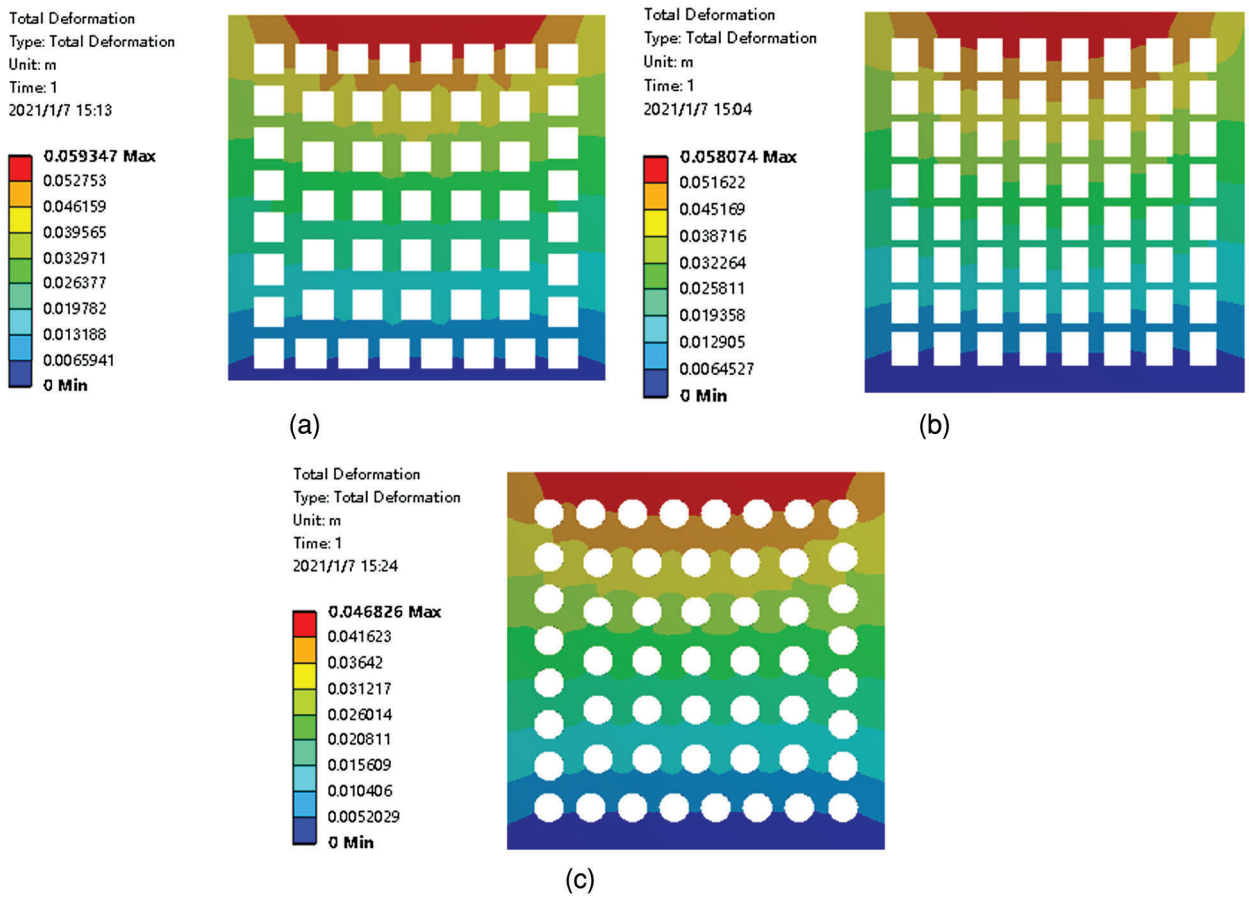

Figure 5: Force diagrams (*z*-direction) for porous ceramics with square (a), strip (b), and circular (c) pores

Table 2: Deformation and normal stress of porous ceramics with different pore types

	Square pores	Strip pores	Circular pores
Deformation (mm)	12.364	8.9379	11.096
Stress (MPa)	1.1409	1.2149	1.0893

Compressive strength is an important parameter for assessing the stability of porous ceramics that are exposed to compressive stresses. The compressive strength increased from ~0.6963 MPa at 2 wt% fiber to ~1.1025 MPa at 6 wt% fiber (Fig. 6b). A lower porosity and uneven pore distribution contributed to stress concentration under an external force, which compromised the material's ability to maintain good resistance and support, thereby affecting the mechanical properties [23]. The porosity was maximized and uniformly distributed at 6 wt% fiber, resulting in less stress concentration and an improved compressive strength. Further addition of fiber to 8 and 10 wt% led to an excess of fibers that caused thinning of the pore wall and partial collapse of the pore structure after sintering. These effects led to a reduction in compressive strength to 0.4953 and 0.2164 MPa, respectively. Overall, the content and distribution of fibers were the main factors affecting the compressive strength of the porous ceramics. Finite element analysis was used to calculate the compressive strength at each porosity (Fig. 6b). The simulated data was consistent with the experimental data, further demonstrating that the model provided an accurate representation of the actual situation.

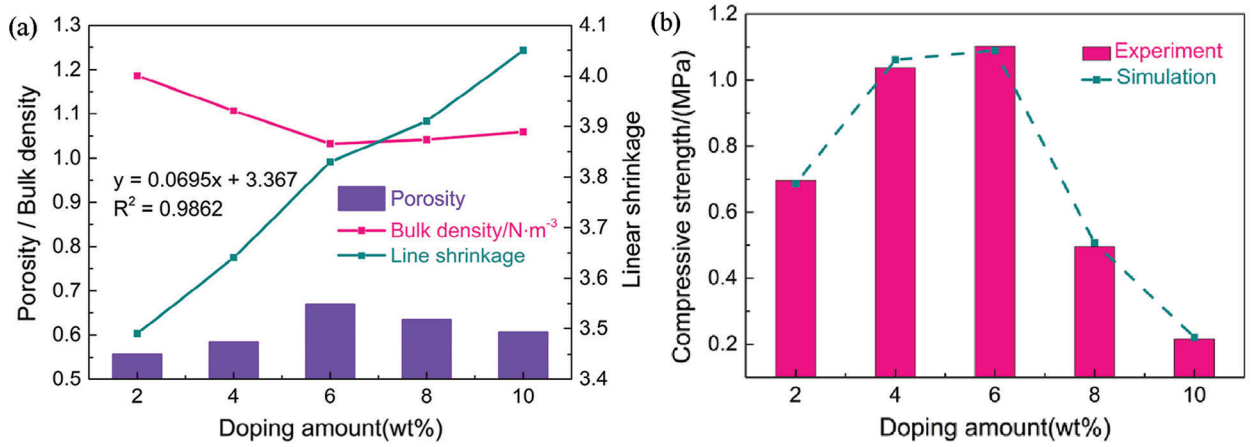

Figure 6: Effect of fiber content on the porosity, bulk density, and compressive strength of the porous ceramics

3.3.4 Effect of Sintering Temperature on Compressive Properties

The effect of sintering temperature is an important factor in the evaluation of the porous ceramics. The porosity decreased with increasing sintering temperature, where the porosity decreased from 66.93% at 950°C to 16.84% at 1100°C (Fig. 7a). This decrease in porosity was attributed to the increase in the content of oxidation-derived silica, as well as partial densification due to slow glass phase flow of the amorphous silica [25]. Specifically, the porosity of the porous ceramics decreased rapidly at sintering temperatures of 1000 and 1100°C. Further, the bulk density generally increased with increasing temperature due to sintering densification [26], where the minimum volume density of 1.0329 g/cm^3 was achieved at 950°C and the maximum of 2.073 g/cm^3 at 1100°C. Sintering at 950°C led to fusing of the grains to form a skeleton while maintaining a small grain size due to the slow kinetics. However, sintering above 1000°C led to faster kinetics and substantial grain growth [27]. A liquid glass phase was formed inside the ceramic, where the effect of surface tension and the migration of liquids led to filling of many internal micropores [28]. This compromised both the porosity and volume, where a maximum linear shrinkage of 24.15% was achieved at 1100°C.

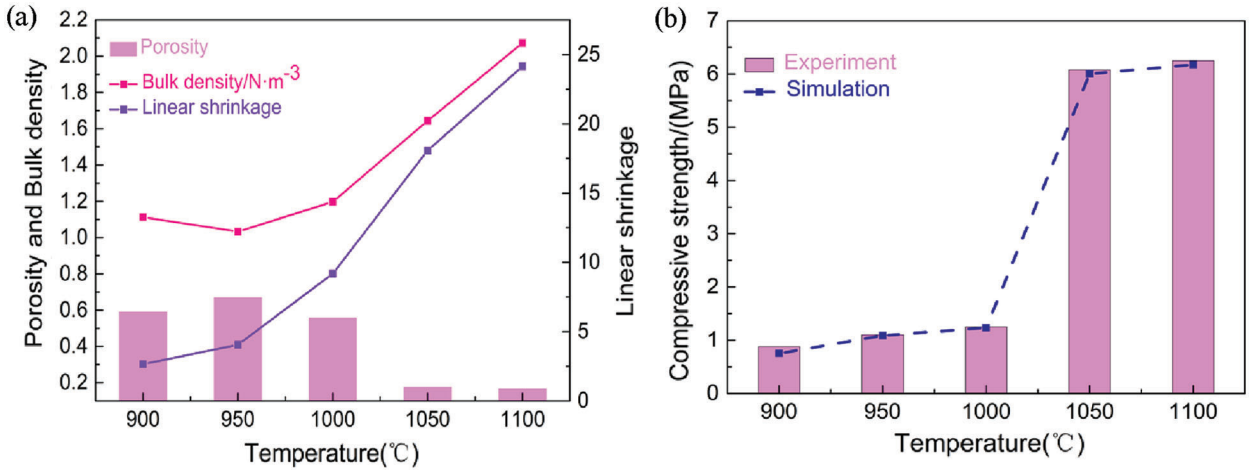

Figure 7: Effect of sintering temperature on the porosity, bulk density, and compressive strength of the porous ceramics

The compressive strength of the porous ceramics increased slightly from 900 to 1000°C (Fig. 7b). Kaolin in the porous ceramic was converted to metakaolin, $2(Al_2O_3 \cdot 2SiO_2) \rightarrow 3Al_2O_3 \cdot 2SiO_2 + 4SiO_2$ [29]. but only the crystal structure was changed at lower temperatures, and no glass liquid phase was produced. The coal gangue gradually formed a mullite-like phase and exhibited liquid phase flow when the temperature was increased to 1000 and 1100°C. $2Al_2O_3 \cdot SiO_2 \rightarrow 2(Al_2O_3 \cdot SiO_2) + SiO_2$ [10]. This led to blocking of a large number of pores, thereby reducing the volume and increasing the compressive resistance. The improved strength was related to the decrease in porosity and the formation of a dense strut between the grains. Further, the increase in mechanical strength corresponded to the decrease in the porosity because coal gangue mainly comprised silica, and partial liquid sintering due to the presence of several alkali impurities in the silica source. Overall, the simulated and experimental compressive strength data exhibited an increase with increasing sintering temperature.

3.4 Thermal Performance Evaluation of Porous Ceramics

Thermal conductivity was used to measure the thermal transfer of different objects. The thermal conductivity of the porous ceramics was characteristic of 1-D heat transfer, where the heat was transferred from the hot end to the cold end. This thermal behavior can be understood based on Fourier's law:

$$\lambda = q \cdot \frac{\delta}{T_1 - T_2} \tag{3}$$

where δ is specimen thickness, T_1 and T_2 represent the temperatures of the hot and cold surfaces, respectively, and q is heat flux.

The thermal impedance (Z_θ) of an interface material can be used to characterize its thermal conductivity, and is defined as the sum of thermal resistance and thermal contact resistance between the interface material and contact surface:

$$Z_\theta = \frac{d}{\lambda \cdot A} + R_i \tag{4}$$

where d is material thickness, λ is heat conduction rate, A is the heat transfer area and R_i is the thermal resistance of the material.

The heat conduction of a porous ceramic is a complex process involving the heat transfer of solid materials, radiation of the pore walls, and convective exchange within the pores. The thermal properties of the porous ceramics were simulated and analyzed using the Fluent module [30]. The simulated gradient change and heat transfer of heat flow in the porous ceramic were evaluated (Fig. 8). The left side of the sample was exposed to a temperature of 950°C and the temperature gradually decreased and reached room temperature by the right side of the sample, thereby completing the primary heat transfer process. The heat flux output near the left and right end holes was larger during heat transfer, and the heat flux perpendicular to the direction of heat flux transmission was larger than that parallel to the direction of heat flux transmission.

3.4.1 Effect of Porosity and Sintering Temperature on Thermal Properties

The porosity of a porous ceramic can affect its heat transfer efficiency and thermal resistance, thereby changing its thermal conductivity. Thermal conductivity typically decreases with increasing porosity, as seen in the various samples sintered at 950°C (Fig. 9a). Specifically, an increase in fiber content from 2 to 6 wt% led to an increase in porosity from 55.74% to 66.93% and a decrease in thermal conductivity from 0.4613 to 0.3919 K(W/m·k). Further, the increase in fiber content to 8 and 10 wt% led to a decrease in porosity to 63.43% and 60.52%, respectively, thus the thermal conductivity increased accordingly to 0.4155 and 0.4399 K(W/m·k), respectively. This behavior was attributed to less resistance to heat transfer as the

distance between the pores decreased [31], thus fiber content directly affected the heat transfer efficiency of the porous ceramics. Relative to the larger surface roughness, the thermal conductivity of the porous ceramic was lower, which significantly increased the thermal resistance. Thus, increasing the porosity as much as possible to optimize the mechanical properties will also lead to an improved thermal performance and energy-saving effect.

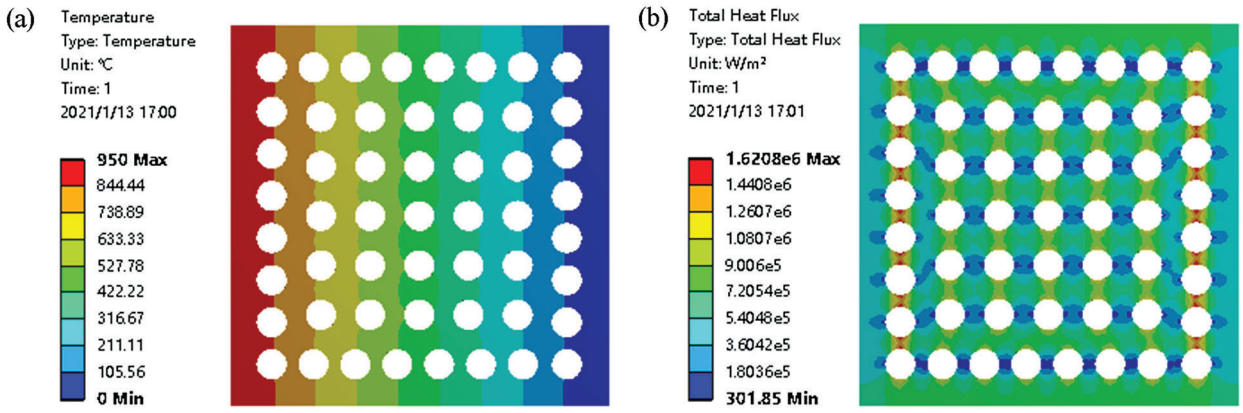

Figure 8: Thermal conductivity of the porous ceramic based on the distribution of temperature (a) and heat flux (b) while exposing the left of the sample to a temperature of 950°C

The thermal conductivity of the porous ceramics produced at different sintering temperatures was evaluated (Fig. 9b). Incomplete volatilization of fibers during sintering at 900°C led to hindered heat conduction, thus the minimum thermal conductivity was 0.3919 K(W/m·k) at 950°C. The coal gangue in the porous ceramics underwent transformation from kaolin to metakaolin between 900 and 1000°C, where only the crystal structure was changed and no glass liquid phase was produced. At temperatures above 1000°C, the components in coal gangue gradually formed a mullite-like phase and exhibited liquid phase flow. This blocked a large number of the pores, and resulted in a smaller volume and higher heat resistance. Further, the hopping of electrons in the ceramics and oxygen vacancies facilitated the transfer of heat at high temperatures, and played an important role in the heat transfer process according to Kronger-Vink notation [32]. Thus, sintering temperature played an important role in determining the thermal properties of the porous ceramics.

3.4.2 Effect of Thermal Impedance

Thermal impedance refers to the heat resistance in the path of heat flow, and provides an indication of the heat transfer ability of a material (Fig. 10). According to the expression of thermal impedance in Eq. (4), the contact thermal impedance is inversely proportional to the thermal conductivity and directly proportional to the thickness of the material. Further, a higher porosity leads to higher contact resistance. Temperature is an important factor in thermal impedance, and is affected by the thermal conductivity. Thus, the thermal conductivity of the porous ceramics at various temperatures can be intuitively determined based on the thermal impedance. The thermal conductivity of porous ceramics decreased due to the lower surface roughness associated with decreasing porosity, which significantly decreased the thermal resistance.

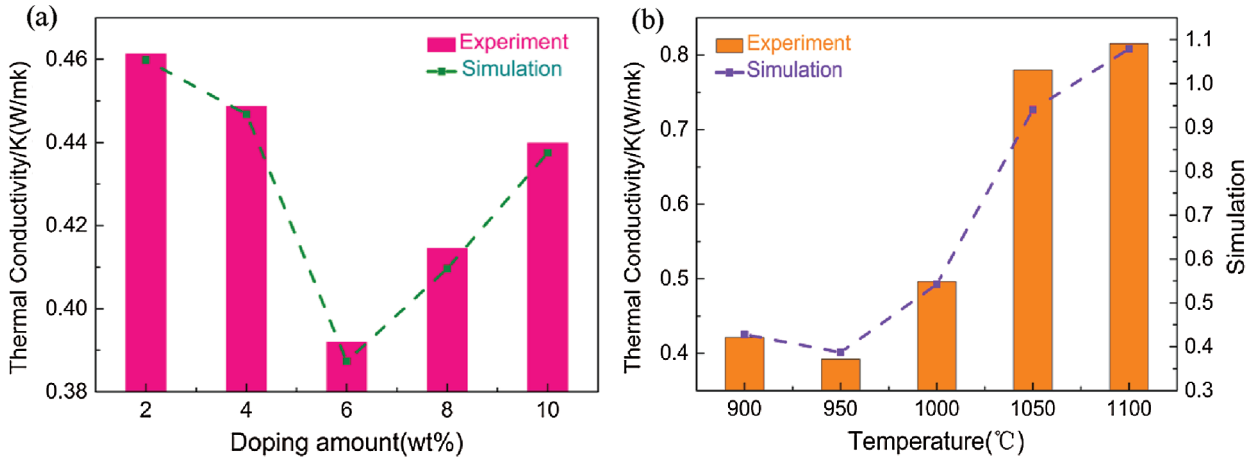

Figure 9: Effects of fiber content (a) and sintering temperature (b) on the thermal conductivity of the porous ceramics

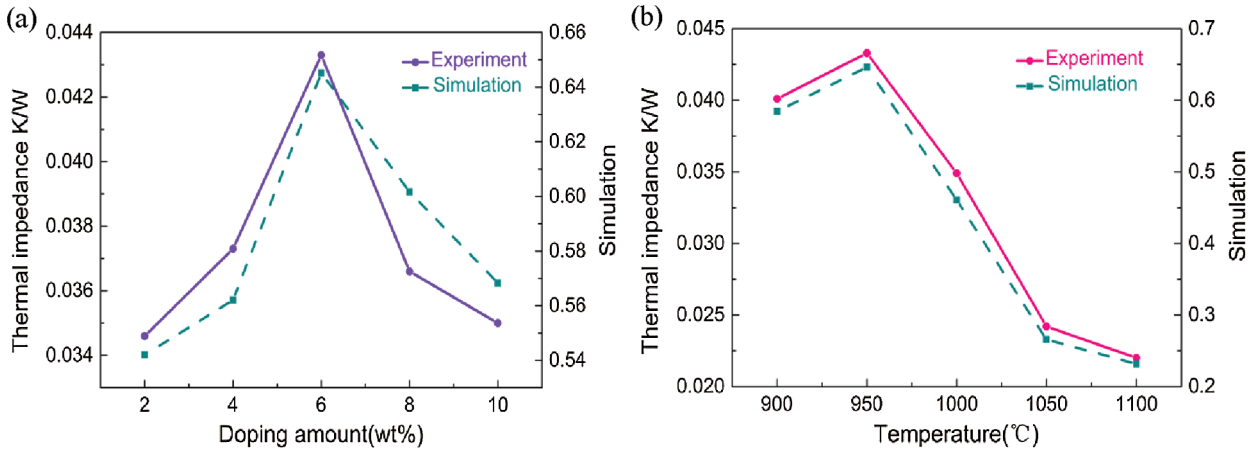

Figure 10: Effect of fiber content (a) and sintering temperature (b) on the thermal impedance of the porous ceramic

4 Conclusions

Highly porous ceramics were prepared using coal gangue and coal slime as raw material, where natural coconut palm fibers served as a pore-forming agent. The main findings of this study are as follows:

1. The maximum apparent porosity and minimum volume density of 66.93% and 1.0329 g/cm^3, respectively, were achieved at a sintering temperature of 950°C.
2. Simulated data revealed that circular pores were the optimal pore shape. Further, the compressive strength increased as the fiber content was increased between 2 and 6 wt%, and subsequently decreased from 8 to 10 wt%. The simulated data were consistent with the experimental data.
3. As the porosity increased from 55.74% to 66.93%, and the equivalent thermal conductivity decreased from 0.4613 to 0.3919 K(W/mk). Further, an increase in sintering temperature from 950 to 1100°C led to an increase in thermal conductivity from 0.3919 to 0.8153 K(W/mk).

Funding Statement: National Natural Science Foundation of China under Grant No. (51372197), Key Innovation Team of Shaanxi Province under Grant No. (2014KCT-04), and Provincial Joint Fund of Shaanxi (2021JLM-28).

Conflicts of Interest: The authors declare that they have no conflicts of interest to report regarding the present study.

References

1. Koshy, N., Dondrob, K., Hu, L., Wen, Q., Meegoda, J. N. (2019). Synthesis and characterization of geopolymers derived from coal gangue, fly ash and red mud. *Construction and Building Materials, 206,* 287–296. DOI 10.1016/j.conbuildmat.2019.02.076.
2. Li, J., Wang, J. (2019). Comprehensive utilization and environmental risks of coal gangue: A review. *Journal of Cleaner Production, 239,* 117946. DOI 10.1016/j.jclepro.2019.117946.
3. Gao, S., Zhao, G., Guo, L., Zhou, L., Yuan, K. (2021). Utilization of coal gangue as coarse aggregates in structural concrete. *Construction and Building Materials, 268,* 121212. DOI 10.1016/j.conbuildmat.2020.121212.
4. Deng, J., Li, B., Xiao, Y., Ma, L., Wang, C. P. et al. (2017). Combustion properties of coal gangue using thermogravimetry–Fourier transform infrared spectroscopy. *Applied Thermal Engineering, 116,* 244–252.DOI 10.1016/j.applthermaleng.2017.01.083.
5. Guo, Y., Zhao, Q., Yan, K., Cheng, F., Lou, H. H. (2014). Novel process for alumina extraction via the coupling treatment of coal gangue and bauxite red mud. *Industrial & Engineering Chemistry Research, 53(11),* 4518–4521. DOI 10.1021/ie500295t.
6. Li, H., Kong, L., Bai, J., Bai, Z., Guo, Z. et al. (2020). Modification of ash flow properties of coal rich in calcium and iron by coal gangue addition. *Chinese Journal of Chemical Engineering*. DOI 10.1016/j.cjche.2020.08.033.
7. Abdel-Gawwad, H. A., Mohammed, M. S., Heikal, M. (2020). Ultra-lightweight porous materials fabrication and hazardous lead-stabilization through alkali-activation/sintering of different industrial solid wastes. *Journal of Cleaner Production, 244,* 118742. DOI 10.1016/j.jclepro.2019.118742.
8. Han, Y., Zhou, L., Liang, Y., Li, Z., Zhu, Y. (2020). Fabrication and properties of silica/mullite porous ceramic by foam-gelcasting process using silicon kerf waste as raw material. *Materials Chemistry and Physics, 240,* 122248. DOI 10.1016/j.matchemphys.2019.122248.
9. Lü, Q., Dong, X., Zhu, Z., Dong, Y. (2014). Environment-oriented low-cost porous mullite ceramic membrane supports fabricated from coal gangue and bauxite. *Journal of Hazardous Materials, 273,* 136–145. DOI 10.1016/j.jhazmat.2014.03.026.
10. Liu, M., Zhu, Z., Zhang, Z., Chu, Y., Yuan, B. et al. (2020). Development of highly porous mullite whisker ceramic membranes for oil-in-water separation and resource utilization of coal gangue. *Separation and Purification Technology, 237,* 116483. DOI 10.1016/j.seppur.2019.116483.
11. Sun, Y., Xue, W. J., Huang, Y., Sun J, L., Zhou, G. Z. (2015). Unidirectional porous alumina ceramics fabricated by freeze-drying process with sodium alginate. *Journal of the Chinese Ceramic Society, 43(6),* 709–715. DOI 10.14062/j.issn.0454-5648.2015.06.01.
12. Yang, M., Guo, Z., Deng, Y., Xing, X., Qiu, K. et al. (2012). Preparation of $CaO–Al_2O_3–SiO_2$ glass ceramics from coal gangue. *International Journal of Mineral Processing, 102,* 112–115. DOI 10.1016/j.minpro.2011.11.004.
13. Geng, J., Zhou, M., Li, Y., Chen, Y., Han, Y. et al. (2017). Comparison of red mud and coal gangue blended geopolymers synthesized through thermal activation and mechanical grinding preactivation. *Construction and Building Materials, 153,* 185–192. DOI 10.1016/j.conbuildmat.2017.07.045.
14. Zhang, Y., Zhang, Z., Zhu, M., Cheng, F., Zhang, D. (2019). Decomposition of key minerals in coal gangues during combustion in O_2/N_2 and O_2/CO_2 atmospheres. *Applied Thermal Engineering, 148,* 977–983. DOI 10.1016/j.applthermaleng.2018.11.113.
15. Ríos-Badrán, I. M., Luzardo-Ocampo, I., García-Trejo, J. F., Santos-Cruz, J., Gutiérrez-Antonio, C. (2020). Production and characterization of fuel pellets from rice husk and wheat straw. *Renewable Energy, 145,* 500–507. DOI 10.1016/j.renene.2019.06.048.

16. Balla, V. K., Kate, K. H., Satyavolu, J., Singh, P., Tadimeti, J. G. D. (2019). Additive manufacturing of natural fiber reinforced polymer composites: Processing and prospects. *Composites Part B: Engineering, 174,* 106956. DOI 10.1016/j.compositesb.2019.106956.
17. Li, J., Shao, G., Ma, Y., Zhao, X., Wang, H. et al. (2019). Processing and properties of polycrystalline cubic boron nitride reinforced by SiC whiskers. *International Journal of Applied Ceramic Technology, 16(1),* 32–38. DOI 10.1111/ijac.13077.
18. Malik, R., Kim, Y. W., Song, I. H. (2020). High interfacial thermal resistance induced low thermal conductivity in porous SiC-SiO_2 composites with hierarchical porosity. *Journal of the European Ceramic Society, 40(3),* 594–602. DOI 10.1016/j.jeurceramsoc.2019.10.056.
19. Kim, Y. H., Kim, Y. W., Seo, W. S. (2020). Processing and properties of silica-bonded porous nano-SiC ceramics with extremely low thermal conductivity. *Journal of the European Ceramic Society, 40(7)*, 2623–2633. DOI 10.1016/j.jeurceramsoc.2019.11.072.
20. Niu, S., Xu, X., Li, X., Chen, X., Luo, Y. (2020). Microstructure evolution and properties of silica-based ceramic cores reinforced by mullite fibers. *Journal of Alloys and Compounds, 829,* 154494. DOI 10.1016/j.jallcom.2020.154494.
21. Mocanu, A. C., Miculescu, F., Miculescu, M., Ciocoiu, R. C., Pandele, A. M. et al. (2021). Comprehensive analysis of compatible natural fibre as sacrificial porogen template for tailored ceramic 3D bioproducts destined for hard tissue reconstruction. *Ceramics International, 47(4),* 5318–5334. DOI 10.1016/j.ceramint.2020.10.113.
22. Du, H., Ma, C., Ma, W., Wang, H. (2018). Microstructure evolution and dielectric properties of Ce-doped $srBi_4Ti_4O_{15}$ ceramics synthesized via glycine-nitrate process. *Processing and Application of Ceramics, 12(4),* 303–312. DOI 10.2298/PAC1804303D.
23. Huang, Q., Liu, T., Zhang, J., He, X., Liu, J. et al. (2020). Properties and pore-forming mechanism of silica sand tailing-steel slag-coal gangue based permeable ceramics. *Construction and Building Materials, 253,* 118870. DOI 10.1016/j.conbuildmat.2020.118870.
24. Guesmi, Y., Lafi, R., Agougui, H., Jabli, M., Oun, A. et al. (2020). Synthesis and characterization of alpha alumina-natural apatite based porous ceramic support for filtration application. *Materials Chemistry and Physics, 239,* 122067. DOI 10.1016/j.matchemphys.2019.122067.
25. Ehtemam-Haghighi, S., Attar, H., Okulov, I. V., Dargusch, M. S., Kent, D. (2021). Microstructural evolution and mechanical properties of bulk and porous low-cost Ti–Mo–Fe alloys produced by powder metallurgy. *Journal of Alloys and Compounds, 853,* 156768. DOI 10.1016/j.jallcom.2020.156768.
26. Wu, J. M., Li, M., Liu, S. S., Shi, Y. S., Li, C. H. et al. (2020). Preparation of porous Al_2O_3 ceramics with enhanced properties by SLS using Al_2O_3 poly-hollow microspheres (PHMs) coated with $casio_3$ sintering additive. *Ceramics International, 46(17),* 26888–26894. DOI 10.1016/j.ceramint.2020.07.165.
27. Wang, Y., Wang, X., Liu, C., Su, X., Yu, C. et al. (2021). Aluminum titanate based composite porous ceramics with both high porosity and mechanical strength prepared by a special two-step sintering method. *Journal of Alloys and Compounds, 853,* 157193. DOI 10.1016/j.jallcom.2020.157193.
28. Pillai, U., Heider, Y., Markert, B. (2018). A diffusive dynamic brittle fracture model for heterogeneous solids and porous materials with implementation using a user-element subroutine. *Computational Materials Science, 153,* 36–47. DOI 10.1016/j.commatsci.2018.06.024.
29. Cao, Z., Cao, Y., Dong, H., Zhang, J., Sun, C. (2016). Effect of calcination condition on the microstructure and pozzolanic activity of calcined coal gangue. *International Journal of Mineral Processing, 146,* 23–28. DOI 10.1016/j.minpro.2015.11.008.
30. Wang, R., Hou, A., Wu, Z. (2020). Tomography-based investigation of flow and heat transfer inside reticulated porous ceramics. *Applied Thermal Engineering, 116115*. DOI 10.1016/j.applthermaleng.2020.116115.
31. Ghafouri, M., Ahn, J., Mourujärvi, J., Björk, T., Larkiola, J. (2020). Finite element simulation of welding distortions in ultra-high strength steel s960 MC including comprehensive thermal and solid-state phase transformation models. *Engineering Structures, 219,* 110804. DOI 10.1016/j.engstruct.2020.110804.
32. Arshad, M., Du, H., Javed, M. S., Maqsood, A., Ashraf, I. et al. (2021). Fabrication, structure, and frequency-dependent electrical and dielectric properties of Sr-doped $BaTiO_3$ ceramics. *Ceramics International, 46(2),* 2238–2246. DOI 10.1016/j.ceramint.2019.09.208.